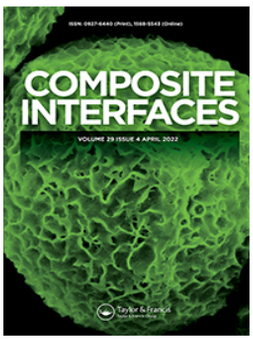

Taylor & Francis
Taylor & Francis Group

Composite Interfaces

ISSN: (Print) (Online) Journal homepage: https://www.tandfonline.com/loi/tcoi20

Simulation of surface asperities on a carbon fiber using molecular dynamics and fourier series decomposition to predict interfacial shear strength in polymer matrix composites

Tanvir Sohail, Sushan Nakarmi, Rebekah Sweat, Ray Baughman, Hongbing Lu & Samit Roy

To cite this article: Tanvir Sohail, Sushan Nakarmi, Rebekah Sweat, Ray Baughman, Hongbing Lu & Samit Roy (2022): Simulation of surface asperities on a carbon fiber using molecular dynamics and fourier series decomposition to predict interfacial shear strength in polymer matrix composites, Composite Interfaces, DOI: 10.1080/09276440.2022.2029314

To link to this article: https://doi.org/10.1080/09276440.2022.2029314

COMPOSITE INTERFACES
https://doi.org/10.1080/09276440.2022.2029314

Taylor & Francis
Taylor & Francis Group

Simulation of surface asperities on a carbon fiber using molecular dynamics and fourier series decomposition to predict interfacial shear strength in polymer matrix composites

Tanvir Sohail[a], Sushan Nakarmi[a], Rebekah Sweat[b], Ray Baughman[c], Hongbing Lu[d] and Samit Roy[a]

[a]Department of Aerospace Engineering and Mechanics, University of Alabama, Tuscaloosa, AL, USA; [b]Department of Industrial & Manufacturing Engineering, Famu-fsu College of Engineering High-Performance,Materials Institute, Florida State University, Tallahassee, FL, USA; [c]Alan G. MacDiarmid NanoTech Institute, University of Texas at Dallas, Richardson, TX, USA; [d]Department of Mechanical Engineering, University of Texas at Dallas, Richardson, TX, USA

ABSTRACT

The objective of this paper is to predict the fiber/matrix interfacial debond strength in composites. Atomic force microscopy (AFM) images of the surface topography of a de-sized carbon fiber reveal that there are surface asperities present at various length scales ranging from a nanometer to several microns. These asperities are likely caused by shrinkage of the polyacrylonitrile (PAN) precursor during the graphitization process. In order to bridge the length scales, a Fourier series-decomposition covering a range of asperity wavelengths and amplitudes is necessary to effectively capture the roughness of the fiber surface at different length scales. Further, once a surface asperity profile has been resolved into individual subcomponents using Fourier-decomposition, MD simulations can then be employed to obtain the interfacial shear strength of the subcomponent asperity of a given amplitude and wavelength. Finally, by recombining the peak interfacial shear force obtained from each of these subcomponents into the overall shear force for the fiber surface profile, the length-scale -averaged shear strength can be obtained for any given asperity. The objective of this paper is to use this novel approach to determine the interfacial shear strength of de-sized carbon fiber embedded in an epoxy matrix and compare predicted results with experimental data.

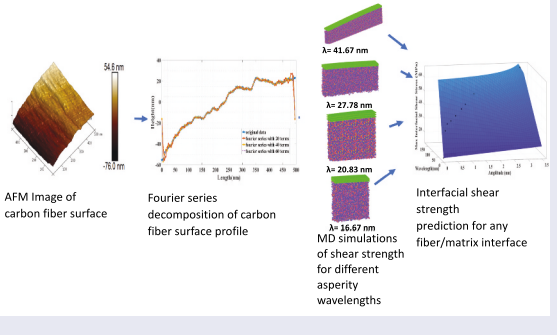

ARTICLE HISTORY

Received 29 October 2021
Accepted 28 December 2021

KEYWORDS

Carbon fiber; polymer composites; asperity; molecular dynamics; multi-scale modeling; epoxy

CONTACT Samit Roy sroy@eng.ua.edu Department of Aerospace Engineering and Mechanics, University of Alabama, Tuscaloosa, AL 35487, USA

1. Introduction

In recent years, fiber-reinforced polymer matrix composites have seen increasing applications in areas, such as aerospace, automotive, wind farms, offshore drilling, sports, and construction. In general, failure in a composite laminate occurs in one of five primary modes: 1) matrix cracking, 2) interfacial debonding between fiber and matrix, 3) fiber fracture in tension, 4) micro buckling of fibers in compression, 5) delamination between adjacent plies. Within a composite, the fiber carries most of the tensile load while the polymer matrix is designed to carry shear and compressive loads. Therefore, in the presence of a transverse matrix crack and/or in the vicinity of a free edge in the laminate, load transfer between fiber and matrix occurs primarily via a shear-lag mechanism at the interface between the fiber and polymer matrix [1,2]. Consequently, the behavior at the fiber–matrix interface (or interphase) with a thickness of around 100 nm plays an important role in determining the stiffness and transverse strength of fiber reinforced composite. In this context, Swadener et al. [3] determined experimentally that the de-bond failure of a glass fiber occurs in the matrix around 3 nm away from the fiber surface. Corroborating this observation, Ding et al. [4] reported that during a fracture event, polycarbonate of a few nanometers thickness remains wrapped around a single-walled carbon nanotube (SWNT) when the SWNT is pulled out of the polycarbonate matrix as a result of crack propagation. Ozkan et al. [5] conducted nano-scale pull-out experiments on individual vapor-grown carbon nanofiber (VGCNF) embedded in epoxy (Epon 828) matrix. Their interfacial shear strength (IFSS) data revealed that high-temperature heat treatment reduces the IFSS of as-grown VGCNFs by as much as 50% due to a significant reduction in the surface roughness and the uneven morphology of the VGCNF, thereby underscoring a clear connection between IFSS and fiber surface roughness.

Consequently, it is very important to investigate the de-bond mechanisms at the fiber–matrix interface in order the improve the interfacial mechanical properties of the composite. An important step in this endeavor is to understand and model the role played by fiber surface roughness and asperities on the interfacial mechanical properties of the composite.

In recent years, researchers have directed considerable effort towards increasing the strength of the bulk polymer matrix by dispersing nanofillers within the matrix [6,7], and/or increasing the interfacial strength between the fiber and the matrix by grafting carbon nanotubes (CNTs) directly on the surface of the carbon fiber [8–19]. The improvement in interfacial strength due to CNT grafting, however, is generally not significant, and CNT grafting often results in a reduction in the in-plane properties of the carbon fiber [20]. The next few paragraphs discuss the typical manufacturing processes employed in producing carbon fibers, in order to shed light on the potential development of surface texture on a carbon fiber during the manufacturing process.

During the industrial manufacture of the polyacrylonitrile (PAN) based carbon fibers, a tow of fiber filaments is fed through a series of heat treatment stages. In the first stage, the precursor PAN fibers are stabilized at temperatures between 200°C and 300°C in the presence of oxygen to generate a structural morphology amenable to high-temperature treatments [21–24]. In the next stage, graphitization of these stabilized fibers is carried out at high temperatures (up to 1600°C) in the presence of inert nitrogen. At the end of the graphitization stage, a fiber with greater than 98 wt% carbon content is produced.

When observed under an electron microscope, the graphitized PAN fiber shows a semi-crystalline morphological structure. The crystalline regions of the semi-crystalline material display graphite-like layers stacked with random orientation relative to each other [25], which are referred to as turbostratic graphitic microstructure in the literature. During the carbonization stage, the emission of volatile products like HCN, NH_3, CO_2, CO, H_2, N_2, H_2O, hydrocarbons, and nitriles [26,27] occur, as impurities like nitrogen, oxygen, and hydrogen are eliminated from the structure. For the manufacture of high-quality carbon fibers, a final step in the graphitization is carried out at temperatures up to 3000°C under noble gas atmosphere, resulting in a fiber that is almost 99 wt% pure carbon [23,28,29]. The graphitization process involves severe mass-loss due to the emission of volatile products, especially in the temperature range between 300 and 500°C, that potentially leads to non-uniform shrinkage in the fiber diameter along its circumference [29–31], thereby giving rise to fairly uniform striations in the fiber axis direction that are only observed on a micron and nano-scale. Researchers have attempted to study and model the fiber-matrix interfacial debonding mechanism as described in the following paragraphs.

For computational modeling of interfacial debonding, a multiscale Voronoi cell finite element approach was developed by Ghosh et al. [32,33] using randomly generated microstructure to analyze composite debond failure. The effect of microstructural randomness on polymer matrix composite (PMC) properties was also studied by Borkowski et al. [34] using finite element analysis (FEA). However, all these fiber–matrix interface modeling studies assume perfectly bonded interface even though there is significant experimental evidence that there exist imperfections in the physical structure of the bond, especially in the absence of chemical functionalization. Consequently, fiber-matrix interactions at the interface are not perfect as assumed by idealized models and could provide locations for damage initiation and propagation due to surface anomalies, such as voids in the carbon fiber [35]. Further, the presence of fiber sizing, combined with a lack of accurate knowledge of its mechanical properties, could further compromise modeling accuracy.

Recently, there has been a lot of interest directed towards investigating the debonded phenomenon and frictional sliding behavior at fiber–matrix interfaces. In this context, it is now well established that structural reliability of composite materials is strongly affected by the debond toughness of the interface between fiber and matrix [36,37]. Understanding the stress transfer mechanism between fiber and matrix across the interface is very important for the application of composites to engineering structures. As alluded to in the previous paragraph, the elastic stress transfer at the interface can be determined along a perfectly bonded region at the fiber matrix interface. On the other hand, stress transfer due to the sliding friction governed by Coulomb's friction law after the interface bond has failed is another important mechanism for load transfer in brittle matrix composites. It has been reported in the literature that interfacial frictional sliding of fibers is a major toughening mechanism that occurs in the crack bridging zone in a composite [36–38]. Hence, progressive debonding and frictional sliding at the interface are of fundamental interest for developing multiscale composite strength prediction models.

In order to characterize the behavior of the interface between the fiber and matrix, single fiber pull-out and/or push-out techniques have been used [39]. From experimental load-displacement curves, initial and peak debond stresses, as well as frictional

pull-out and/or push-out stresses, can be extracted. For this purpose, analytical models have been developed to provide a theoretical basis for the determination of the interfacial properties from experimental data [39–41]. Although most earlier models did not consider the roughness (asperity) of the debonded interface to have a pronounced effect on the interfacial frictional sliding behavior, more recent studies have considered this effect analytically and/or experimentally. For fiber push-out, Jero et al. [42] were among the first to observe that when a single fiber is pushed, a pushback phenomenon that results in a 'reseating load drop' occurs. Carter *et al.* [43], using a fiber pull-out test, were able to confirm the results presented in [42]. The effects of fiber-matrix interfacial roughness and residual axial strain in the fiber were included by Kerans et al. [44] to predict the load-displacement behavior for relatively large sliding displacements. However, the sliding displacements are relatively small in many crack-bridging problems. Therefore, the analysis in [44] was extended to include effects of interfacial roughness by introducing a friction parameter [45]. The effect of interfacial roughness on the frictional sliding using fiber push-out and push-back tests on a model composite of Plexiglas rods in an epoxy matrix was also studied [46]. Further, Mackin *et al.* [47,48] developed an analytical model of fiber sliding for the push-out problem. With the help of MD simulations Verma et al [49] showed that geometrical imperfections such as wrinkles and ripples helps in enhancement of interfacial properties of bi-crystalline graphene /polyethylene system providing a clear indication of asperity effect at the nanoscale. Despite the plethora of opportunities to further investigate the effect of asperity on polymer -nanofiller interface at the nanoscale, very few studies have been conducted so far. One of the reasons could be attributed to the lack of potentials to mimic experimental behavior observed near polymer interfaces. To address this issue Verma et al [50] have provided a detailed review regarding the different types of potential that can be employed to model polymer nanocomposites in MD domain and have discussed the challenges that can be encountered using the classical mechanics-based approach. Lu et al [51] utilized Dreiding potential to model a system of polyethylene nanocomposites with carbon based nanofillers using the united atom model to represent the chains of hydrocarbon. The united atom technique helps in reduction of atoms in the system and allows for simulating larger systems without increasing the computational complexity or expense. But unlike reactive potentials like ReaxFF or AIREBO, Dreiding potential does not allow chemical bond formation and breakage which can be a serious draw back when depicting a realistic system in MD. Rahman et al [52] used AIREBO and PCFF interatomic potentials for simulation of graphene and polymer interface. Although AIREBO is more computationally efficient reactive potential than ReaxFF and significantly reduces the simulation time, yet it is unable to accurately portray the experimental data for epoxy system as pointed out in [53]. As a result of this not many publications can be found on polymers utilizing AIREBO potential. Mattson et al [53] also reported that ReaxFF had a longer range of validity for experimental data. Hence ReaxFF with appropriate parameters can be used for polymer nanocomposite study. This statement is further validated by Odegaard et al [54] who showed close agreement between experimental and predicted MD values of mechanical stiffness and strength when used for epoxy system utilizing ReaxFF parameterization of Liu et al [55].

Despite the numerous research investigations as mentioned above, closing of the knowledge gap in the modeling the exact geometry of the roughness or asperity at the fiber–matrix interface remains elusive. A more rigorous model for a single fiber pull-out with a rough interface using a Fourier series approach was presented by Liu et al. [56]. Assuming that the interface between fiber and matrix has been completely debonded, they were able to derive the solutions of fiber pull-out stress and relative displacement along the interface. In addition, their analysis was extended to the case of fiber push-out in terms of asperity wear to simulate the change of the frictional push-out stress during fiber sliding [57]. The main advantage of the Fourier series representation of the asperity is that it can accommodate surface roughness profile spanning multiple length scales unlike earlier studies. More recently, Stupkiewicz [58] proposed a model of an interface with micro-dilatancy in which the radial misfit varies and depends on the relative displacement by extending the model of a strip on a frictional foundation; as a result, irreversible effects of wear of asperities can be included for large sliding distances or for cyclic loading. The potential effects of interfacial roughness in ceramic matrix composites were studied by Parthasarathy et al. [59] using a model that included a progressively increasing contribution of roughness. Following Liu et al. [56], a robust Fourier-series based fiber push-out prediction model that can handle any type of surface roughness and that can also accommodate fiber residual thermal stresses in the radial and axial direction was developed by Chai et al. [39]. However, in [39] the average wavelength and the maximum amplitude of the roughness at the steel fiber/epoxy interface was assumed, and not actually measured from atomic force microscopy (AFM) data.

Consequently, the objective of this paper is to apply the Fourier-series technique to define surface asperities measured using AFM on an un-sized carbon fiber, and then use this information, in conjunction with molecular modeling, to predict the interfacial shear strength at a fiber–matrix interface in a carbon-epoxy composite. The decision to use de-sized carbon fiber was primarily made to facilitate molecular modeling due to the lack of precise knowledge regarding sizing constituents and their properties. Although this paper primarily investigates the shear stress transfer at the interface, some amount of thermal transport also occurs at the interface as pointed out in [60], and bi-crystalline graphene–polymer interface enhances this thermal transport. The effect of bi-crystallinity on stress transfer and thermal transport will be investigated in our future work.

2. Methods/experimental

2.1 AFM imaging of asperities on carbon fiber surface

As alluded to in the introduction, the surface features of carbon fiber and the adhesion to a matrix is driven by the manufacturing conditions, including temperature, surface treatments, and sizing application [61–63]. In this section, the de-sized carbon fiber surface is analyzed using AFM that reveals the surface profile and nano-roughness that can be quantified by the mean roughness (Ra) and the root mean square roughness (Rq) [62]. The surface roughness has been shown to

decrease with increased temperature during the oxidation process of the carbon fiber [64,65]. Carbon fiber precursor and spinning conditions early in the manufacturing process also contribute to the final fiber morphology due to the consolidation processes [66]. The interfacial adhesion is not only influenced by the roughness but also the chemical composition, additives to the surface, as well as compatibility with the matrix [67,68].

In this study, IM7 carbon fibers were de-sized using a burning technique to observe the true surface morphology of the fiber surface without the addition of manufacturer sizing that is applied to the fiber to protect the filaments and increase compatibility to the matrix in composites. AFM of the IM7 fiber surface seen in Figure 1(a) was performed using the Veeco Instruments Inc. Multimode AFM with nano-scope V (Plainview, NY) with a scan size of 500 nm, scan rate of 0.977 Hz, and 128 scan lines. Scanning electron microscopy (SEM) in Figure 1(b) was performed using a Thermo Fisher Scientific Helios G4 UC (Waltham, MA). The surface of the IM7 seen in Figure 1 shows relatively uniform striations in the axis direction that are only seen on a micron and nanoscale. The AFM data is shown in Table 1, acquired from the analysis of Figure 1(a), includes surface profile information including Ra (6.21 nm) and Rq (7.93) which are in line with expectations of similar fibers and scanned size. It should be noted that contrary to the model presented in [35], the presence of voids on the carbon fiber surface were not experimentally observed using AFM or SEM

The surface profile perpendicular to the fiber axis obtained using AFM is shown in Figure 2 where multiple sections to show fiber profile data consistency. Three 500 nm scans and two 200 nm scans were taken of the 500 nm square AFM image as shown in Figure 2(a). The profile shown in Figure 2(b) was used for model development via Fourier series decomposition to incorporate varied length-scales of surface roughness. Additional model verification was performed using another set of asperity data from Figure 2(a) as discussed in Section 3.1.

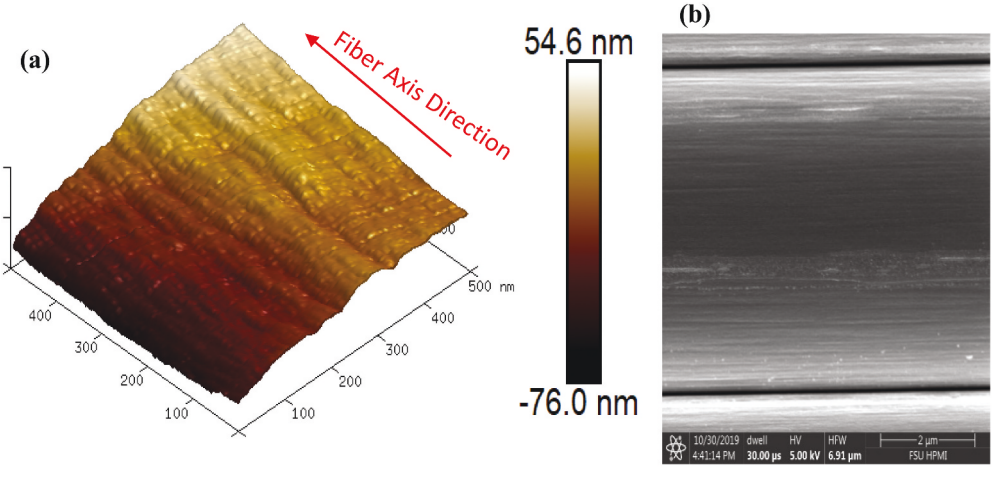

Figure 1. (a) AFM image showing de-sized IM7 carbon fiber surface morphology over a 500 nm^{2}area and (b) SEM image showing the full diameter of the IM7 carbon fiber surface including axially oriented striations.

Table 1. AFM data for carbon fiber surface roughness as shown in Figure 1(a).

Results	
Mean	0.000137 nm
Standard Deviation	21.1 nm
Z Range	101 nm
Surface Area	267,000 nm^2
Projected Surface Area	250,000 nm^2
Surface Area Difference	6.80%
Rq	7.93 nm
Ra	6.21 nm
Roughness Rmax	46.6 nm
Skewness	−0.249
Kurtosis	3.03

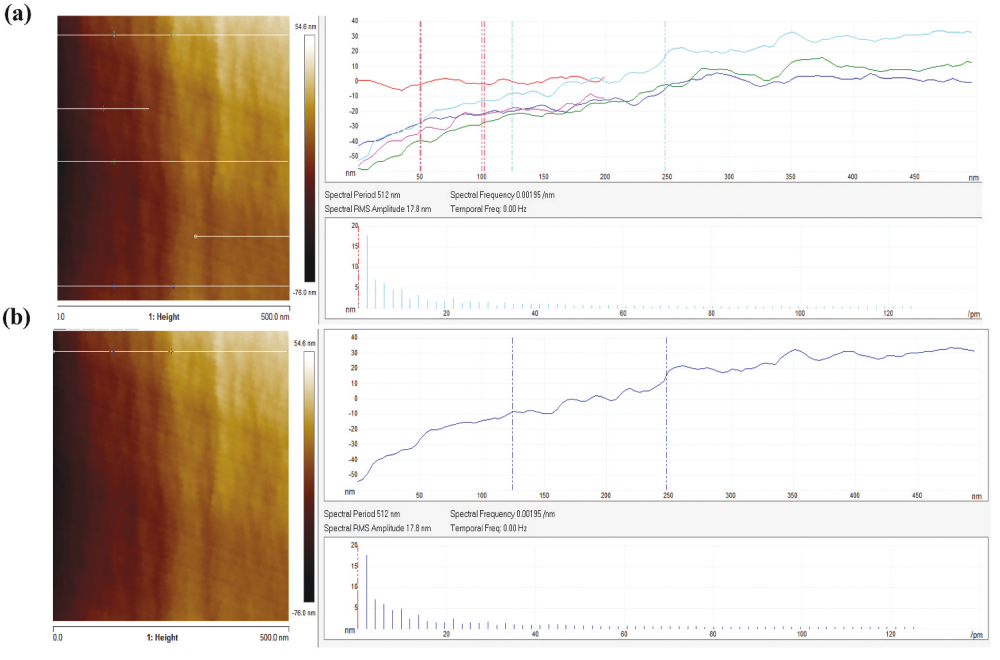

Figure 2. AFM image showing de-sized IM7 carbon fiber surface and line scans of surface texture along the fiber circumference at different locations along the fiber axis.

2.2. Model development

2.2.1 Best-Fit line to fiber surface image

The multiscale surface roughness representation approach begins with acquiring the surface roughness profile over a circumferential length of 500 nm from Figure 2(b). The circumferential tilting of the surface data is removed by using a best fit line, as shown in Figure 3. After removing the tilting, Fourier transformation is applied as described in Section 2.2.2 The Fourier series describes the surface as a superposition of cosine terms of different amplitude, wavelength, and phase angle. The asperity height (h(x)) is then represented as the sum of the best fit and the Fourier Series as discussed below.

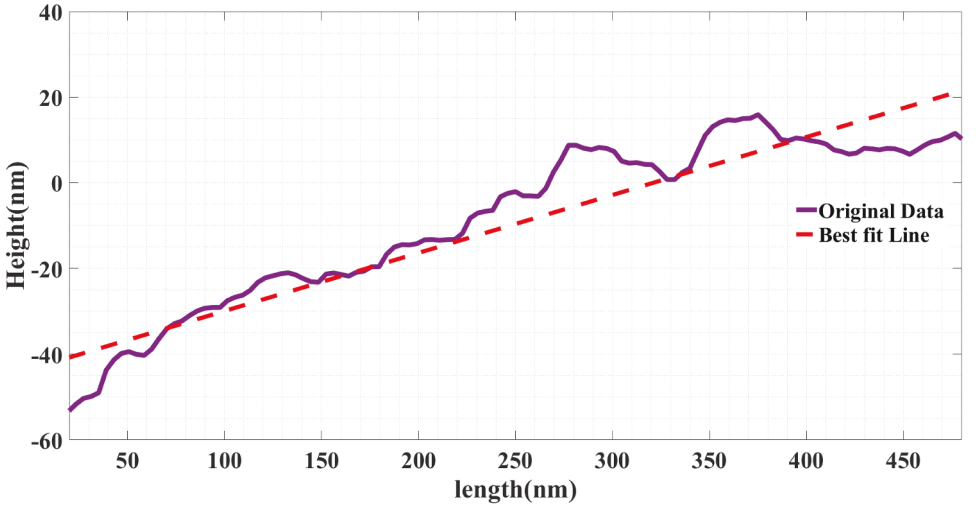

Figure 3. Best–fit line to AFM data from Figure. 2(b).

2.2.2 *Asperity modeling using fourier series*

Assuming that the total asperity height h(x) is given by,

$$h(x) = ax + b + \sum_{n=1}^{N} C_n \cos(\frac{n\pi x}{L} - \varphi_n), -L \le x \le L \tag{1}$$

where, x is measured along the circumference of the fiber, **a** and **b** are known constants of the linear fit to the surface tilt, 2 L is the circumferential length under consideration, N is the total number of terms in the series, and φ_n is the phase angle associated with the n^{th} Fourier cosine series term. From basic trigonometry,

$$\sum_{n=1}^{N} C_n \cos(\frac{n\pi x}{L} - \varphi_n) = C_n \sin(\varphi_n).\sin\left(\frac{n\pi x}{L}\right) + C_n \cos(\varphi_n).\cos\left(\frac{n\pi x}{L}\right) \tag{2}$$

Defining $a_n = C_n \sin(\varphi_n) \text{and} b_n = C_n \cos(\varphi_n)$, Eqn. (1) can be rewritten as

$$y(x) = h(x) - ax - b = \sum_{n=1}^{N} a_n \sin\left(\frac{n\pi x}{L}\right) + b_n \cos\left(\frac{n\pi x}{L}\right) \tag{3}$$

The coefficients a_n and b_n in Eqn. (3) can be obtained by using the principle of orthogonality,

$$a_n = \frac{1}{L}\int_{-L}^{L} y(x).\sin(\frac{n\pi x}{L})dx$$

$$b_n = \frac{1}{L}\int_{-L}^{L} y(x).cos\left(\frac{n\pi x}{L}\right)dx$$

2.2.3 Derivation of incremental shear force in the Z-direction due to interfacial shear between fiber and matrix

Consider an infinitesimal force dF_Z in the fiber axial direction (z-direction) due to interfacial shear stress $\tau_Z(x)$ caused by the mechanical interlocking between the matrix and the fiber surface roughness resisting axial sliding motion, as depicted in Figure 4. Assuming that the thickness of the slice of fiber in the fiber axial direction is designated as **t**, and the infinitesimal circumferential arc as ds, we get

$$dF_Z = t\tau_Z(x)ds \tag{4}$$

But from differential geometry for RCC, $ds^2 = dx^2 + dy^2 = dx^2 + \left(\frac{dy}{dx}\right)^2 dx^2$

or,

$$ds = \sqrt{\left[1 + \left(\frac{dy}{dx}\right)^2\right]}dx \tag{5}$$

Substituting Eqn. (5) in (4) and integrating from -L to L provides the total longitudinal force F_z necessary for sliding to occur along the fiber–matrix interface bounded by the circumferential length 2 L and axial length t in Figure 4., given by,

$$F_z = \int_{-L}^{L} dF_z = t\int_{-L}^{L} \tau_Z(x)\sqrt{\left[1 + \left(\frac{dy}{dx}\right)^2\right]}dx \tag{6}$$

Where, τ_Z (x) is the maximum interfacial shear stress which varies with circumferential position x due to asperities, but is assumed to remain uniform along the axial length, t. From Eqn. (3),

$$\frac{dy}{dx} = \sum_{n=1}^{N} \frac{n\pi}{L} a_n \cos\left(\frac{n\pi x}{L}\right) - \frac{n\pi}{L} b_n \sin\left(\frac{n\pi x}{L}\right) \tag{7}$$

Substituting Eqn. (7) in (6),

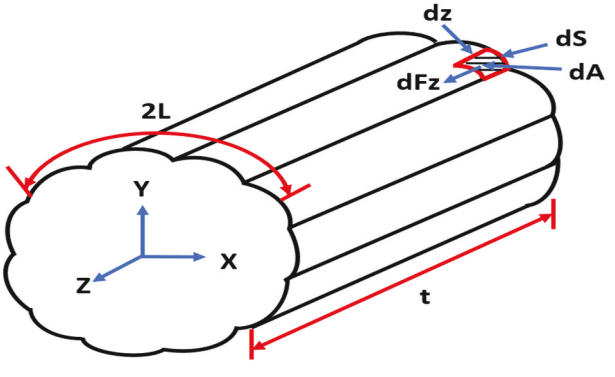

Figure 4. A schematic showing a single carbon fiber with asperities along a longitudinal section of length t and circumferential width 2 L.

$$F_z = t\int_{-L}^{L} \tau_Z(x)\sqrt{\left[1+\left(\sum_{n=1}^{N}\frac{n\pi}{L}a_n\cos\left(\frac{n\pi x}{L}\right)-\frac{n\pi}{L}b_n\sin\left(\frac{n\pi x}{L}\right)\right)^2\right]}dx \tag{8}$$

From Eqn. (8)

$$F_z = t\int_{-L}^{L} \sqrt{\left[\tau_z^2(x)+\left(\sum_{n=1}^{N}\tau_Z(x)\frac{n\pi}{L}a_n\cos\left(\frac{n\pi x}{L}\right)-\frac{n\pi}{L}b_n\sin\left(\frac{n\pi x}{L}\right)\right)^2\right]}dx \tag{9}$$

Equation (9) cannot be solved without quantifying the magnitude and distribution of the unknown maximum shear stress $\tau_Z(x)$ within the representative area element (RAE) shown in Figure 4. However, assuming that there is a characteristic shear strength τ_{Zn} corresponding to each Fourier-decomposed asperity subcomponent of amplitude C_n and wavelength $\frac{4L}{n}$, we can postulate that $\tau_Z(x)$ can be expressed as the circumferentially length-averaged shear strength for each individual asperity amplitude and its corresponding wavelength, mathematically represented by

$$\tau_Z(x) \;=\; \frac{\sum_{n=1}^{N}\tau_{Zn}\frac{n\pi}{L}\left[a_n\cos\left(\frac{n\pi x}{L}\right)-b_n\sin\left(\frac{n\pi x}{L}\right)\right]}{\sum_{n=1}^{N}\frac{n\pi}{L}a_n\cos\left(\frac{n\pi x}{L}\right)-\frac{n\pi}{L}b_n\sin\left(\frac{n\pi x}{L}\right)} \tag{10}$$

Where, τ_{Zn} is the characteristic maximum shear stress for a single wave-shaped asperity of amplitude C_n and wavelength $\frac{4L}{n}$ to be obtained using molecular dynamics (MD) simulations as described in the next section. Further, it can be shown that in the limit as asperity amplitude C_n tends to zero, then $\lim_{C_n\to 0}\tau_{Zn}\to\tau_b$, which is the non-zero baseline shear strength of a fiber (independent of x and n) when surface asperity is negligibly small, and substituting this in Eqn. (10) yields $\lim_{C_n\to 0}\tau_Z(x)\to\tau_b$. Substituting Eqn. (10) in Eqn. (9) and integrating provides the value of the critical force at slippage, F_{zc}, in the fiber axial direction caused by the surface roughness resisting sliding motion in the fiber axial direction for the configuration shown in Figure 4, given by

$$F_{zc} = t\int_{-L}^{L}\sum_{n=1}^{N}\tau_{Zn}\frac{n\pi}{L}\left[a_n\cos\left(\frac{n\pi x}{L}\right)-b_n\sin\left(\frac{n\pi x}{L}\right)\right]\sqrt{\left[1+\frac{1}{\left(\sum_{n=1}^{N}\frac{n\pi}{L}a_n\cos\left(\frac{n\pi x}{L}\right)-\frac{n\pi}{L}b_n\sin\left(\frac{n\pi x}{L}\right)\right)^2}\right]}dx \tag{11}$$

2.2.4 Numerical integration using the gaussian quadrature

The complicated form of the integral in Equation (11) mandates use of numerical integration, such as, Gaussian quadrature [69]. Assigning M Gauss points along the circumferential length, 2 L, of the fiber under consideration and changing the limits of the integral in Equation (11) from -L to L to −1 to 1 in order to satisfy the Gaussian quadrature requirements, we get,

$$\bar{x} = \frac{x}{L} \tag{12}$$

$$dx = L\, d\bar{x} \tag{13}$$

$$F_{zc} = tL \int_{-1}^{1} \sum_{n=1}^{N} \tau_{Zn} \frac{n\pi}{L} \left[a_n \cos\left(\frac{n\pi\bar{x}\mathrm{L}}{L}\right) - b_n \sin\left(\frac{n\pi\bar{x}\mathrm{L}}{L}\right) \right] \sqrt{\left[1 + \frac{1}{\left(\sum_{n=1}^{N} \frac{n\pi}{L} a_n \cos\left(\frac{n\pi\bar{x}\mathrm{L}}{L}\right) - \frac{n\pi}{L} b_n \sin\left(\frac{n\pi\bar{x}L}{L}\right) \right)^2} \right]} d\bar{x} \tag{14}$$

Using Gaussian quadrature,

$$F_{zc} = tL \sum_{k=1}^{M} \left[\sum_{n=1}^{N} \tau_{zn} \left[\frac{n\pi}{L} a_n \cos\left(\frac{n\pi\bar{x}_k L}{L}\right) - b_n \sin\left(\frac{n\pi\bar{x}_k L}{L}\right) \right] \sqrt{\left[1 + \frac{1}{\left(\sum_{n=1}^{N} \frac{n\pi}{L} a_n \cos\left(\frac{n\pi\bar{x}_k L}{L}\right) - \frac{n\pi}{L} b_n \sin\left(\frac{n\pi\bar{x}_k L}{L}\right) \right)^2} \right]} \right] w_k \tag{15}$$

Where,w_k are the Gaussian weights, and $\bar{x}_k$ are the Gaussian integration points. Finally, the average maximum shear stress (i.e., the shear strength) of the interface, averaged over a length t along the fiber axis for any given asperity shape and length scale in the circumferential direction can be obtained as,

$$\tau_{ZAvg}^{Max} = \frac{F_{zc}}{t \times 2L} \tag{16}$$

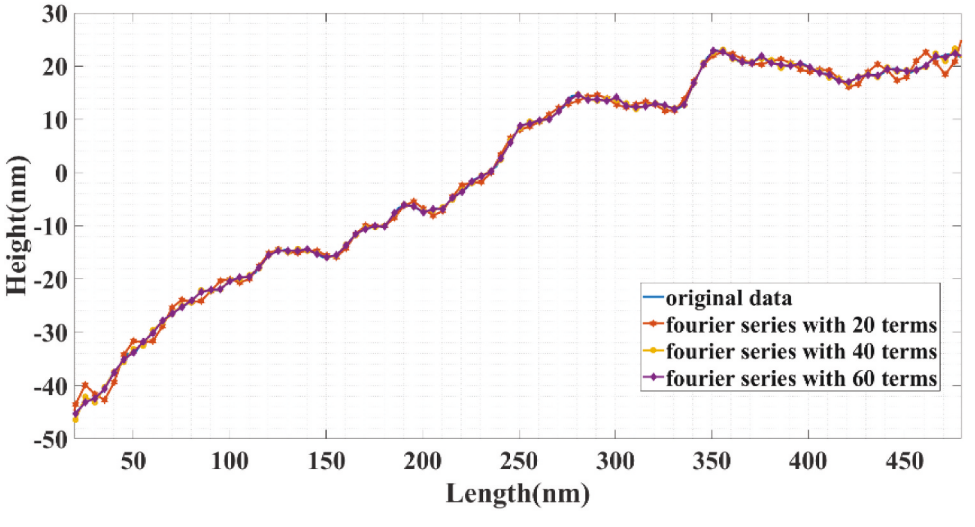

Figure 5. Graph showing the convergence of mean square error vs. number of Fourier series terms.

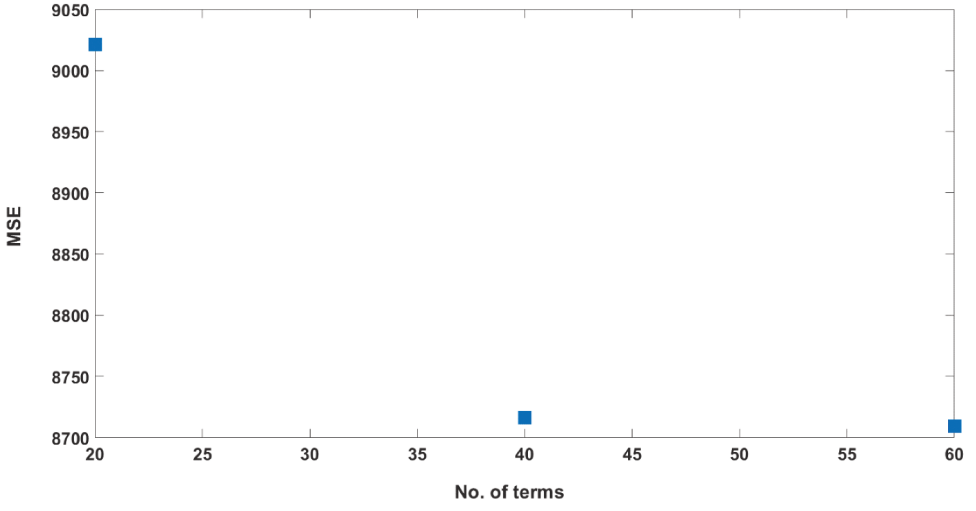

Figure 6. Graph depicting improving accuracy of Fourier series representation of AFM data with increasing number of terms.

It can be observed from Figure 5 that a good fit to the AFM data is obtained with a Fourier series containing 60 terms (N = 60). In order to further validate this, a mean square error (MSE) plot is shown in Figure 6. It can be seen, with an increasing number of terms in the Fourier Series, the error between the experimentally measured value of asperity and that predicted using the Fourier series rapidly diminishes.

In this paper, the circumferential width used in the analysis is $2L$ = 500 nm, and axial length t = 500 nm, based on the dimensions of the scanned AFM image in Figure 2.

It should be noted that an exact representation of the fiber surface roughness would require a double Fourier series decomposition using cosine and sine series in x and z in the domain bounded by 2 L and t, as depicted in Figure 4. However, since the fiber diameter shrinkage due to heat-treatment results in fairly uniform striations in the fiber axial direction [29–31] as depicted in Fig 1(b), only a one-dimensional Fourier decomposition in the fiber circumferential direction is employed. Strictly speaking, the average interfacial shear strength (IFSS) thus obtained is valid only over the fiber axial length, t, over which the circumferential asperity profile is assumed to remain uniform. However, an accurate estimate of the IFSS for the entire fiber can be obtained by applying the proposed methodology to obtain IFSS for circumferential roughness profiles at different locations along the fiber axis with individual segmental length t_i, i = 1, m, and then averaging over the m segmental IFSS values.

Based on the best fit to the AFM asperity data, the Fourier series employed in Eqn. (15) contains 60 terms, where each term has a unique amplitude C_n and wavelength λ_n. In order to obtain the maximum interfacial shear stress contribution, τ_{Zn},corresponding to the surface roughness represented by each Fourier series term, molecular dynamics (MD) simulation is employed to simulate the interaction between a carbon fiber with asperity amplitude C_n and wavelength λ_n, and the epoxy matrix. In the interest of computational efficiency, eleven selected values of this series with their corresponding amplitude C_n and wavelength λ_n are employed in the MD simulations and are listed in Table 2. Details of the MD simulations are described in Section 2.2.5

2.2.5 Molecular dynamics simulation to obtain average maximum shear stress for various asperity length-scales

Because it is computationally impractical to perform MD simulation for every one of the sixty Fourier series terms, therefore, it was decided to include selected terms from the 60 terms used in the fit to the asperity data, and then model its specific surface profile in MD to obtain the maximum shear stress. Hence, a total of 10 MD simulations were performed, for n = 6,12,18,24,30,36,42,48,54, and 60 as listed in Table 2, and the maximum interfacial shear stress, τ_{Zn}, for each of these terms was obtained. The maximum interfacial shear stress for the terms not included were subsequently obtained using nonlinear interpolation between the 10 simulation data points, which will be discussed later in Section 3. Also, a separate MD simulation was performed using a single flat graphene sheet to obtain the baseline maximum interfacial shear stress in the absence of asperities on the carbon fiber.

The atomistic simulations presented here were conducted using the open-source platform Large-scale Atomic/Molecular Massively Parallel Simulator (LAMMPS). Figure 7 shows the first case study performed using MD, for n = 6. Initially, a representative volume element (RVE) of EPON-862/DETDA polymer with dimension 11.8 nm ×10.8 nm× 5.0 nm was created with 30,223 atoms and periodic in all directions. Periodic boundary conditions allowed the use of NPT ensemble during MD simulation. The density of this polymer block was computed to be 1.21 g/cm^3 which is in good agreement with the measured density of EPON-862 (1.17–1.2 gm/cc) at 300 K. This polymer block was further replicated along the X direction to incorporate the Fourier decomposed asperity the carbon fiber given by the half wavelength of Fourier series data for the 6th term with C_6 = 3.33 nm and wavelength λ_6 = 166.67 nm (see Table 2), as shown in Figure 7. It should be noted that utilizing symmetry of the cosine wave, only one half-wavelength (λ_6 /2 = 83.34 nm) was modeled using MD in the interest of computational efficiency. As pointed out in the introduction, ReaxFF with appropriate set of parameters can be used for a thermoset polymer system. Therefore, two sets of ReaxFF parameters were used for modelling the system including the graphene sheets and the polymer in our study. The parameters of [70] was used for modelling and equilibrating the graphene sheets before their placement over the polymer, whereas all simulations involving polymer were conducted using the parameters from Liu [55]. In ReaxFF,

Table 2. Selected list of Fourier series amplitudes and wavelengths to be analyzed using MD.

Cases	Amplitude (C_n) (nm)	a_n	b_n	Wavelength, $\lambda = \frac{4L}{n}$ (nm)
Baseline	0	0	0	Infinity
n = 6	3.33	−1.58	−2.93	166.67
n = 12	1.92	0.09	−1.92	83.33
n = 18	1.28	−0.03	−1.28	55.56
n = 24	0.93	0.08	−0.93	41.67
n = 30	0.76	0.03	−0.76	33.33
n = 36	0.53	−0.05	−0.53	27.78
n = 42	0.35	−0.01	−0.35	23.81
n = 48	0.21	0.02	−0.21	20.83
n = 54	0.13	−0.02	−0.13	18.52
n = 60	0.09	−0.09	−0.01	16.67

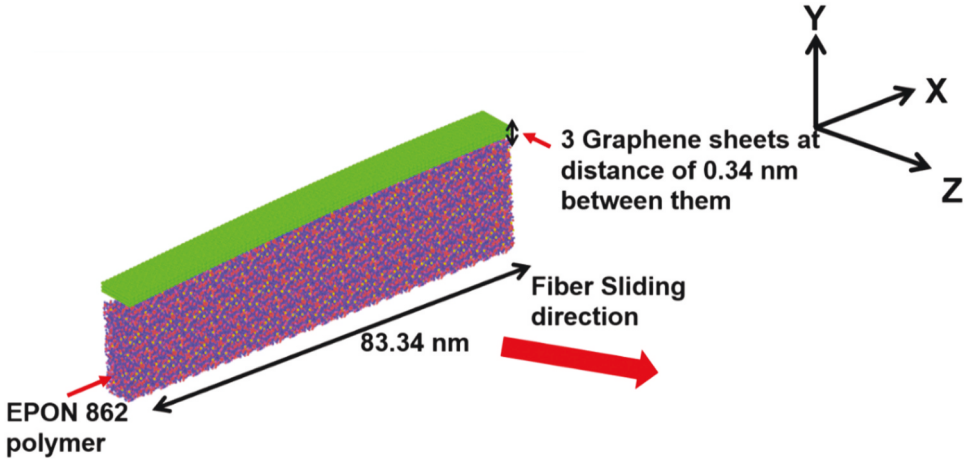

Figure 7. Case study using MD simulation of asperity at the interface between carbon fiber and polymer matrix. Three graphene sheets are stacked together to simulate the carbon fiber.

all covalent interaction depends on the bond order function. Bond-order is a function of the interatomic distance between the atoms. It goes to zero when the inter-atomic distance between a pair of atom exceeds the covalent bond distance signifying breakage of a bond. Hence, ReaxFF can be used to model a system where breakage and formation of bonds occur. The extended polymer block has the dimensions of 83.34 nm× 11.8 nm × 5 nm in X, Y, and Z directions, respectively, as shown in Figure 7.

The carbon fiber surface for this case study was modeled using three layers of graphene sheets upholding the distance equivalent to the Van der Waal's radius of interaction between them and shaping them to the cosine wave contour corresponding to the amplitude and wavelength defined in Table 2 for n = 6, created with help of a MATLAB code. At the fiber–matrix interface, the polymer was made to conform with the contour of the carbon fiber surface. Hence, the top surface of the polymer block was modified into a shape of a cosine function with the amplitude corresponding to that of n = 6 in Table 2 by removing selected molecules from the polymer system, instead of deleting individual atoms and leaving behind free radicals. The removal of molecules was done using an in-house developed MATLAB code. In this way, it was ensured that there was no spurious dissociation of atoms from surface of the polymer, especially at 300 K. The fiber surface for this case represents the Fourier decomposed roughness on the surface of carbon fiber at nanoscale for the Fourier series term with n = 6. The graphene sheets were then placed over the top surface of the polymer block maintaining a distance equivalent to the Van der Waal's radius of interaction, as depicted in Figure 7. Therefore, it is assumed that there is no chemical bonding at the fiber matrix interface, as is usually the case of a de-sized carbon fiber and epoxy matrix.

The entire system of graphene sheets and polymer block was equilibrated corresponding to its minimum energy configurational state before proceeding with sliding of the graphene sheets relative to the polymer block to obtain the

maximum shear stress. The minimization was achieved by first performing energy minimization in LAMMPS using its built-in conjugate gradient algorithm. The minimization was carried out for 0.5 ps with time-step of 0.1 fs. During this interval, the temperature of the system approached 0 K, attaining its most stable state. Thereafter, the temperature of the graphene-polymer system was elevated through a steady-stepped equilibration process using the NPT ensemble with an initial pressure of 0.1 atm. The equilibration was performed by raising the system successively to 30 K, 77 K, 150 K, 230 K, 270 K for 2 ps and finally to 300 K for 5 ps and then allowing the system to rest in order to permit volumetric expansion. This allows the system to achieve a stable energy state at 300 K devoid of any thermally induced stresses or distortions of graphene sheets and the polymer. The total equilibration time was 15 ps with a time-step of 0.1 fs. The graphene sheets were modeled as an undulated rigid body to prevent any presence of thermally induced wrinkles during the thermalization process. After the convergence of the potential energy (PE) during equilibration, the energy minimized, thermally equilibrated system was subjected to the sliding of the graphene sheet relative to the polymer at 300 K using NPT ensemble at an initial pressure of 0.1 atm. The graphene sheets were imparted a uniform velocity of 2.5 m/s and made to slide along the Z direction for a period of 0.3ps. Periodic boundary conditions were used in all three directions. Periodic conditions were applied along the sliding direction (Z direction), thereby maintaining continuity of the graphene sheets across that boundary, and hence mimicking the sliding of a continuous carbon fiber. No covalent bonding was observed between the graphene atoms and polymer surface atoms; only non-bonded Van der Waals interaction existed between them. In the case of MD simulation for the baseline case, similar boundary conditions and the procedure as outlined above were adopted, except that the three graphene sheets were allowed to remain completely flat without any asperities. However, in order to make a fair comparison with the other cases studied here, the flat graphene sheets were prevented from having any thermally induced wrinkles by using the 'fix rigid' command in LAMMPS.

2.2.6 Computation of maximum interfacial shear stress for the n^{th} term

The tangential forces on graphene sheets along the pulling direction that were obtained during the sliding of the graphene sheets was used for the computation of the maximum interfacial shear stress, τ_{zn}, between the graphene and polymer substrate for each of the asperity term listed in Table 2. The tangential forces can be directly obtained for each atom in the MD system from the Lammps dump files at each instance of sliding displacement. The dump files were post processed using an in-house MATLAB code. With the help of this code, the tangential forces on all the atoms in the three-graphene sheet were identified and summed up to obtain the total tangential force on the graphene sheets. This force was then divided by the contact area between the graphene sheets and the polymer surface to obtain the Interfacial Shear Stress as described in [71] and as shown in Eqn .17. For the sake of computational simplicity, the contact area, A, in Eqn. 17 was calculated by taking the length of the graphene sheet along the x-axis multiplied with the contact width of the graphene sheets and the polymer substrate.

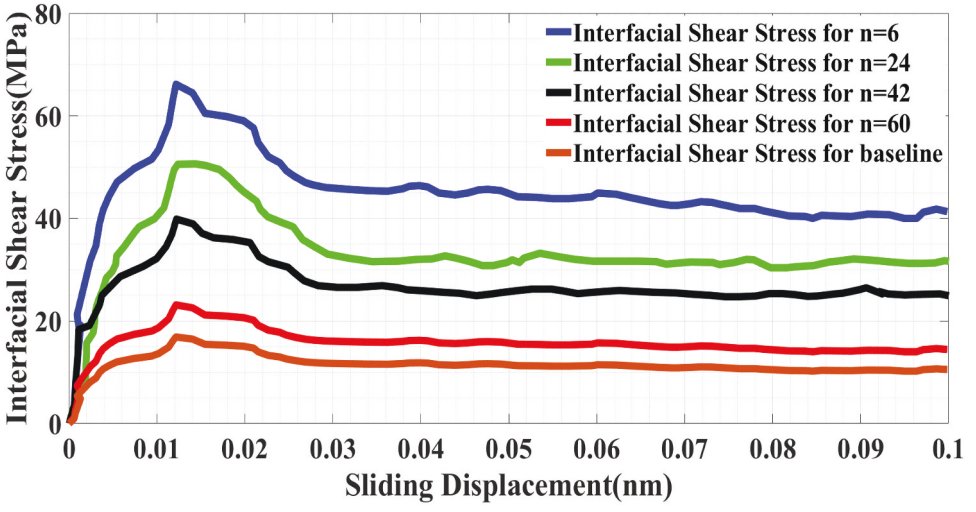

Figure 8. Variation of interfacial shear stress with respect to the displacement of the graphene sheet obtained from MD simulation for the case n = 6,24,42,60 and the baseline case.

$$\tau_{zn} = \frac{F_z}{A} \tag{17}$$

Eqn. (17) was used to obtain the maximum interfacial shear stress between the carbon fiber–epoxy interface using MD for the selected values of n listed in Table 2. Figure 8 shows the variation of interfacial shear stress with sliding displacement of the graphene sheets obtained using Eqn. (17) for five cases from Table 2 (n = 6,24,42,60 and the baseline case). It can be seen from Figure 8 that for all of the asperity amplitude cases studied, the interfacial shear stress (IFSS) reaches a maximum value and then it plateaus to a value of about 30% lower than the maximum, once the graphene sheets have overcome the static resistance and the sliding resistance comes into effect. Further, the maximum value of the IFSS is directly proportional to the amplitude of the asperity. Only non-bonded interactions between graphene and epoxy are modeled here using Lennard-Jones and Coulomb potentials. Similar trend is observed for all the asperity cases in Table 2, and therefore, due to space constraint we have only chosen five representative cases as displayed in Figure 8. It is also evident that the periodic boundary condition plays an important role in the trend shown in the IFSS plot as it does not go to zero with increasing sliding displacement. This is different than what is reported in most of the literature where complete pullout of the graphene sheets is simulated using MD, and hence their IFSS is reduced to zero [72,73] upon pull-out. The peak values of IFSS in Figure 8 are recorded in Table 3 as the maximum interfacial shear stress, τ_{Zn}, for each asperity amplitude.

3. Results and discussion

As mentioned in Section 2.2.5, due to the computationally intensive nature of the simulations, it is impractical to perform MD simulation for each one of the sixty Fourier series terms. Therefore, MD simulations were selectively performed for only the terms listed in Table 2 and the maximum interfacial shear stress (τ_{Zn}) corresponding to each

Table 3. Maximum interfacial shear stress obtained for selected terms of the Fourier series decomposition.

Cases	Amplitude (C_n) (nm)	a_n	b_n	Wavelength (λ) (nm) $\frac{4L}{n}$	τ_{zn} (MPa) (from MD simulations)
Baseline	0	0	0	Infinity	15.06
n = 6	3.33	−1.58	−2.93	166.67	66.17
n = 12	1.92	0.09	−1.92	83.33	60.55
n = 18	1.28	−0.03	−1.28	55.56	56.72
n = 24	0.93	0.08	−0.93	41.67	50.45
n = 30	0.76	0.03	−0.76	33.33	47.85
n = 36	0.53	−0.05	−0.53	27.78	43.44
n = 42	0.35	−0.006	−0.35	23.81	40.12
n = 48	0.21	0.02	−0.21	20.83	38.26
n = 54	0.13	−0.02	−0.13	18.52	33.45
n = 60	0.09	−0.09	−0.014	16.67	23.14

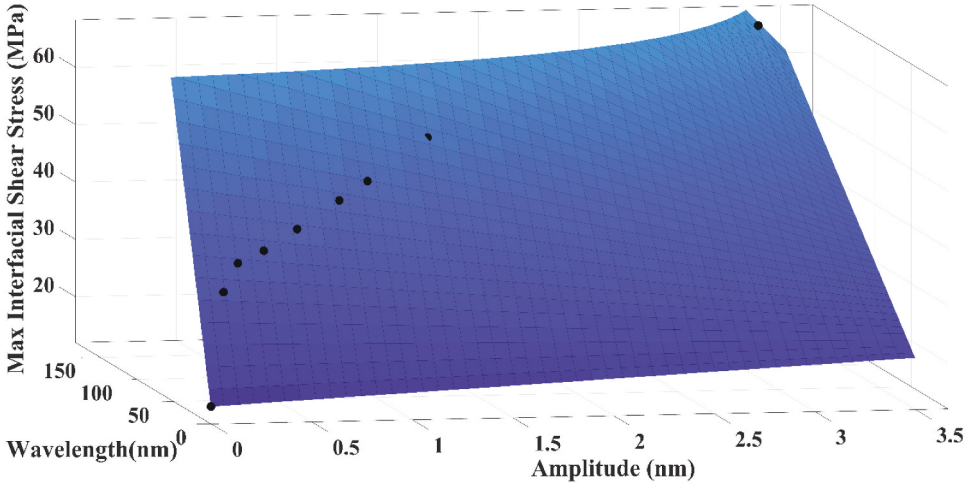

Figure 9. Nonlinear surface fit to MD data points obtained using Eqn. (18).

term was tabulated in the last column of Table 3. An interpolation was then performed for τ_{Zn} as a function of asperity amplitude (C_n), and asperity wavelength (λ_n), as depicted in Figure 9, to obtain the missing maximum interfacial shear stress for remaining terms not listed in Table 3. The non-linear interpolation was performed using MATLAB software to obtain a relationship between maximum interfacial shear stress (τ_{Zn}), the asperity amplitude (C_n) and asperity wavelength (λ_n) using an equation of the form,

$$\tau_{Zn} = \tau_b + p_1 C_n + p_2 \lambda_n + p_3 C_n \lambda_n \tag{18}$$

Where, τ_b is the baseline maximum interfacial shear stress obtained using MD simulations and tabulated in Table 3. The coefficients p_1,p_2 *and* p_3 were obtained using least squared fit to the data in Table 3 with 95% confidence bounds. The optimum values of the 3 fit parameters were obtained as $p_1 = 1.682$ MPa nm^{-1}, $p_2 = 0.9853$ MPa nm^{-1} and $p_3 = -0.2163$ MPa nm^{-2} at an R-square value of 95.04% and an RMSE of 4.24. Equation (18) enables the bridging of length scales, as it uses nanoscale data from MD simulations to obtain interfacial shear strength for a spectrum of asperity sizes ranging from the nanoscale to the microscale.

3.1 Prediction of interfacial shear strength based on asperities data

In this section, the AFM-based fiber surface asperity data set at a specific axial location from Figure 3 (data set 1) and τ_{Zn} from Table 3 are used in conjunction with Eqn. (15), (16) and (18) to predict the interfacial shear strength of a carbon fiber/epoxy system with known surface asperity. The convergence characteristics for the total force at slippage in the fiber axial direction, F_z, determined from Eqn. (15) as a function of the number of Gauss points is shown in Figure 10. As can be observed, excellent convergence is achieved for 3 or more Gauss quadrature points.

The converged value of F_z = 13,097,969.19 × 10^{-12} N as obtained from Figure 10. Using Eqn. (16) with L = 250 × 10^{-9} m, t = 500 × 10^{-9} m we obtain, τ_{ZAvg}^{Max} = 52.39 MPa for dataset 1.

In order to validate the method for an independent set of AFM data taken at a different fiber axial location, AFM surface profile data (data set 2) for the same de-sized carbon fiber was used as shown in Figure 11. As before, the circumferential tilting of this data was again removed using a best fit line and a similar Fourier decomposition method was used to obtain the surface as a summation of sine and cosine terms. Figure 12 shows the excellent Fourier series fit to the asperity data for data set 2. The same procedure as outlined for data set 1 was used to obtain F_z as well as τ_{ZAvg}^{Max}. However, instead of performing MD simulations to obtain the maximum interfacial shear stress for data set 2, the interpolation function in Eqn. (18) was utilized to obtain τ_{Zn} for each of the 60 terms of the Fourier series due to the fact that the fiber-matrix material system has remained the same.

Figure 13 shows the convergence of the maximum axial force F_z as a function of Gauss points used. As can be observed, excellent convergence is achieved for 3 or more Gauss quadrature points. The converged value of F_z = 13,453,554.06 × 10^{-12} N as shown in Figure 13. Using Eqn. (16) with L = 250 × 10^{-9} m, b = 500 × 10^{-9} m, we obtain τ_{ZAvg}^{Max} = 53.81 MPa for dataset 2. Taking the average of the predicted τ_{ZAvg}^{Max} at these two different locations along the fiber axis provides a rough estimate of the IFSS for the entire fiber–matrix interface, given by $\overline{\tau_{ZAvg}^{Max}}$ = 53.10 MPa. The results are summarized in Table 4.

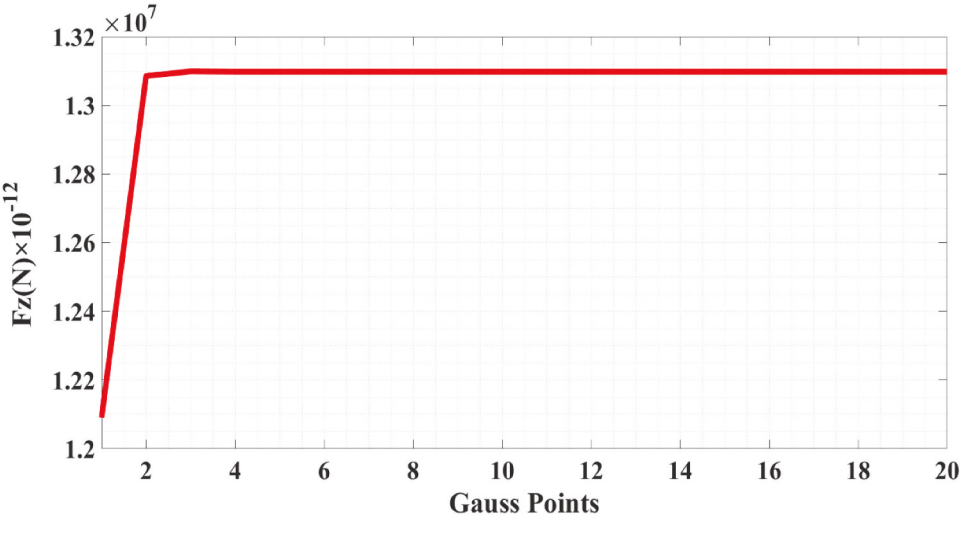

Figure 10. The convergence in F_z obtained for data set1 as a function of number of Gauss points.

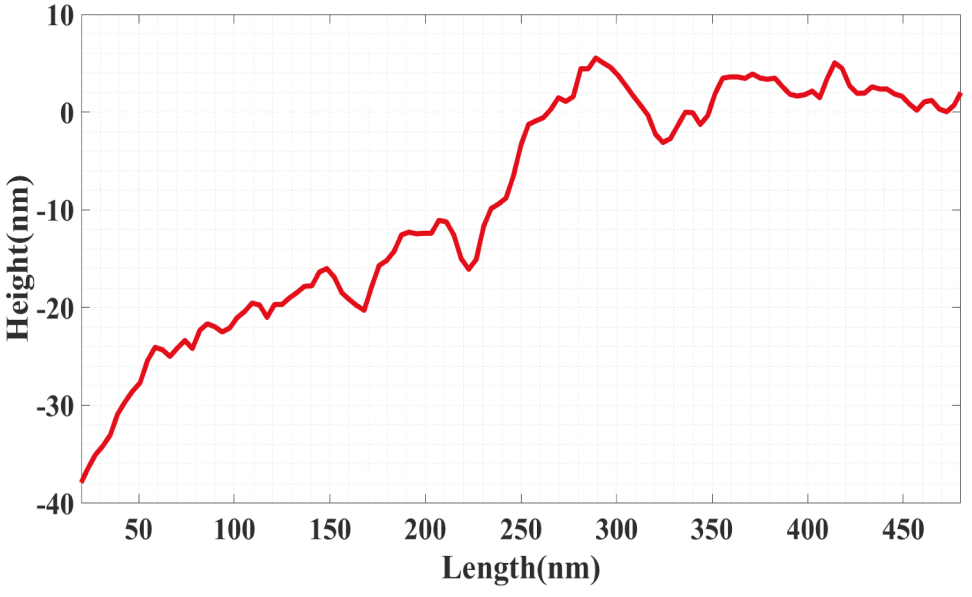

Figure 11. AFM profile for data set 2.

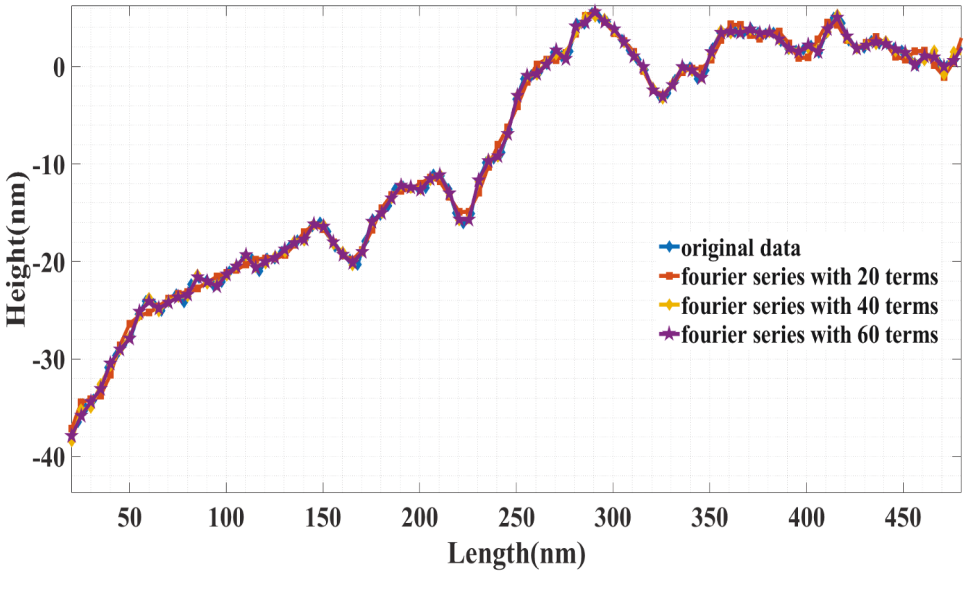

Figure 12. Fourier series fit for data set 2 for model verification.

It can be seen from Table 4, the average IFSS value obtained is in reasonable agreement with the experimentally obtained IFSS data presented by Ozkan et al. [5] using nano-scale pull-out tests performed on VGCNF with a surface roughness of 1–2 nm embedded in EPON 828 epoxy matrix. They reported an IFSS value of 66 ± 10 MPa, following a high-temperature heat treatment on as-grown VGCNF, which is about 19.5% higher than our

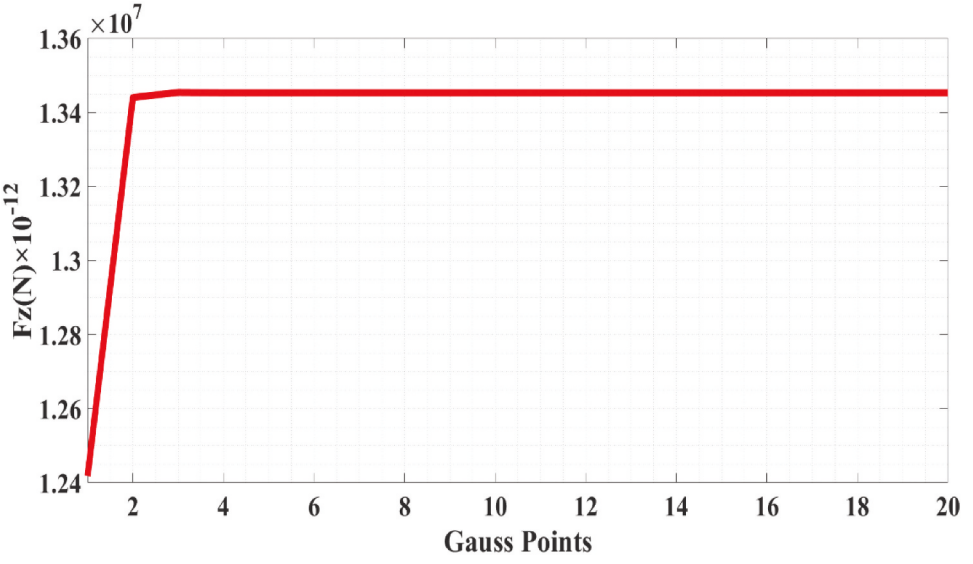

Figure 13. The convergence in F_z obtained for data set- 2.

Table 4. Comparison of interfacial shear strength between experimental and predicted values.

	Shear Stress τ_z (MPa)	Percentage difference from the experimental value
Predicted IFSS using the model	53.1	-
Experimental Value [Ref 74]	43.1	−23.1
Experimental Value [Ref 5]	66.0	19.5

predicted value. An IFSS value of 43.12 MPa for unsized T800H carbon fiber with Ra = 16.34 nm was reported in [74], using the single fiber fragmentation test. The ~23% difference in the predicted value from these experimental values of IFSS is likely due to the fact that the epoxy resin system used in Ref [5] is Hexion EPON 828, and in Ref [74] it is LY-1 (from China) and is somewhat different from the Hexion EPON 862 epoxy system modeled using MD in this paper, thereby resulting in a difference in the surface energy interactions between the fiber and the epoxy matrix.

4. Conclusions

In this paper, AFM images of the surface topography of a de-sized carbon fiber revealed that there are surface asperities present at various length scales ranging from a nanometer to several microns. These asperities are likely caused by shrinkage of the polyacrylonitrile (PAN) precursor during the oxidation and graphitization process. In order to bridge the length scales, a Fourier series decomposition covering a range of asperity wavelengths and amplitudes was employed to effectively capture the roughness of the fiber surface. Further, surface asperity profiles resolved into individual subcomponents using Fourier decomposition were then modeled using molecular dynamics simulations to obtain the interfacial shear strength of the subcomponent asperity of a given amplitude and wavelength. Finally, by recombining the interfacial shear force

obtained from each of these subcomponents into the overall shear force for the fiber surface profile, the length-scale-averaged shear strength was obtained for any given asperity.

The values of predicted IFSS obtained using this procedure for a de-sized carbon fiber embedded in epoxy are in reasonable agreement with the experimentally obtained IFSS for de-sized carbon/epoxy reported in [74] using the single fiber fragmentation test. Additional corroboration is obtained from IFSS data for VGCNF embedded in EPON 828 matrix. Therefore, the paper has proposed and demonstrated a proof-of-concept for a novel approach to determine the IFSS of de-sized carbon fiber embedded in an epoxy matrix using a Fourier series decomposition to bridge the length scales. More work is needed to extend this approach to sized carbon fiber and to carbon fiber tows. The introduction of functionalized covalent bonds between the fiber and matrix is also feasible within the modeling framework. Future work will entail introducing a carbon nanotube sheet in the MD simulations to predict the interfacial shear strength and compressive strength of CNT overwrapped carbon fibers, as discussed in detail by the authors in [20]. Our future study will also incorporate the effect of grain boundaries in polycrystalline graphene sheets on the interfacial shear strength to simulate polycrystalline carbon fiber surface.

Acknowledgments

The authors would like to acknowledge the sponsorship of this research by NSF Scalable Nanomanufacturing (SNM) Program, grant number CMMI-1636306, with Dr. Khershed Cooper as Program Director.

Disclosure statement

No potential conflict of interest was reported by the author(s).

Funding

This work was supported by the National Science Foundation [CMMI-1636306].

References

[1] McManus HL, Maddocks JR. On microcracking in composite laminates under thermal and mechanical loading polymer. Polym Compos. 1996;4(5):305–314.
[2] Nairn JA, Mendels DA. On the use of planar shear-lag methods for stress-transfer analysis of multilayered composites. Mech Mater. 2001;33(6):335–362.
[3] Swadener JG, Liechti KM, Lozanne ALD. The intrinsic toughness and adhesion mechanisms of a glass/epoxy interface. J Mech Phys Solids. 1999;47(2):223–258.
[4] Ding W, Eitan A, Fisher FT, et al. Direct observation of polymer sheathing in carbon nanotube–polycarbonate composites. Nano Lett 2003;3(11):1593–1597.
[5] Ozkan T, Chen Q, Chasiotis I. Interfacial strength and fracture energy of individual carbon nanofibers in epoxy matrix as a function of surface conditions. Compos Sci Technol. 2012;72(9):965–975.

[6] Hussain F, Hojjati M, Okamoto M, et al. Review article: polymer-matrix nanocomposites, processing, manufacturing, and application: an overview. J Compos Mater. 2006;40 (17):1511–1575.
[7] Thostenson ET, Li C, Chou T. Nanocomposites in context. Compos Sci Technol. 2005;65 (3):491–516.
[8] Jia J, Zhao J, Xu G, et al. A comparison of the mechanical properties of fibers spun from different carbon nanotubes. Carbon. 2011;49(4):1333–1339.
[9] Frankland SJV, Harik VM. Analysis of carbon nanotube pull-out from a polymer matrix. Surf Sci. 2003;525(1):L103–L108.
[10] Qian H, Bismarck A, Greenhalgh ES, et al. Carbon nanotube grafted carbon fibres: a study of wetting and fibre fragmentation. Compos Part A Appl Sci Manuf. 2010;41(9):1107 14.
[11] Chowdhury SC, Okabe T. Computer simulation of carbon nanotube pull-out from polymer by the molecular dynamics method. Compos Part A Appl Sci Manuf. 2007;38(3):747–754.
[12] Sager RJ, Klein PJ, Lagoudas DC, et al. Effect of carbon nanotubes on the interfacial shear strength of T650 carbon fiber in an epoxy matrix. Compos Sci Technol. 2009;69(7):898–904.
[13] Fang C, Zhao J, Jia J, et al. Enhanced carbon nanotube fibers by polyimide. Appl Phys Lett. 2010;97(18):181906.
[14] Grimmer CS, Dharan CKH. Enhancement of delamination fatigue resistance in carbon nanotube reinforced glass fiber/polymer composites. Compos Sci Technol. 2010;70 (6):901–908.
[15] Mei L, He X, Li Y, et al. Grafting carbon nanotubes onto carbon fiber by use of dendrimers. Mater Lett. 2010;64(22):2505–2508.
[16] Zhang FH, Wang RG, He XD, et al. Interfacial shearing strength and reinforcing mechanisms of an epoxy composite reinforced using a carbon nanotube/carbon fiber hybrid. J Mater Sci. 2009;44(13):3574–3577.
[17] Godara A, Gorbatikh L, Kalinka G, et al. Interfacial shear strength of a glass fiber/epoxy bonding in composites modified with carbon nanotubes. Compos Sci Technol. 2010;70 (9):1346–1352.
[18] Siddiqui NA, Sham ML, Tang BZ, et al. Tensile strength of glass fibres with carbon nanotube–epoxy nanocomposite coating. Compos Part A Appl Sci Manuf. 2009;40 (10):1606–1614.
[19] Zhang YC, Wang X. Thermal effects on interfacial stress transfer characteristics of carbon nanotubes/polymer composites. Int J Solids Struct. 2005;42(20):5399–5412.
[20] Kokkada P, Roy S, Unnikrishnan V, et al. A multiscale model to study the enhancement in the compressive strength of multi-walled cnt sheet overwrapped carbon fiber composites. Compos Struct. 2019;219:170–178.
[21] Bajaj P, Roopanwal AK. Thermal stabilization of acrylic precursors for the production of carbon fibers: an overview. J Macromol Sci C Polym Rev. 1997;37(1):97–147.
[22] Fitzer E, Frohs W, Heine M. Optimization of stabilization and carbonization treatment of PAN fibres and structural characterization of the resulting carbon fibres. Carbon. 1986;24 (4):387–395.
[23] Rahaman MSA, Ismail AF, Mustafa A. A review of heat treatment on polyacrylonitrile fiber. Polym Degrad Stabil. 2007;92(8):1421–1432.
[24] Ruhland K, Frenzel R, Horny R, et al. Investigation of the chemical changes during thermal treatment of polyacrylonitrile and 15 N-labelled polyacrylonitrile by means of in-situ FTIR and 15 N NMR spectroscopy. Polym Degrad Stabil. 2017;146:298–316.
[25] Frank E, Steudle LM, Ingildeev D, et al. Carbon fibers: precursor systems, processing, structure, and properties. Angew Chem Int Ed. 2014;53(21):5262–5298.
[26] Goodhew PJ, Clarke AJ, Bailey JE. A review of the fabrication and properties of carbon fibres. Mater Sci Eng. 1975;17(1):3–30.
[27] Jain MK, Abhiraman AS. Conversion of acrylonitrile-based precursor fibres to carbon fibres. J Mater Sci. 1987;22(1):278–300.
[28] Johnson JW, Marjoram JR, Rose PG. Stress graphitization of polyacrylonitrile based carbon fibre. Nature. 1969;221(5178):357–358.

[29] Manocha LM, Bahl OP, Jain GC. Length changes in PAN fibers during their pyrolysis to carbon fibers. Angew Makromol Chem. 1978;67(1):11–29.
[30] Lee S, Kim J, Ku BC, et al. Structural evolution of polyacrylonitrile fibers in stabilization and carbonization. ACES. 2012;2(2):275–282.
[31] Gutmann P, Will JM, Kurt S, et al. Carbonization of polyacrylonitrile-based fibers under defined tensile load: influence on shrinkage behavior, microstructure, and mechanical properties. Polym Degrad Stab. 2019;163:174–184.
[32] Ghosh S, Lee K, Raghavan P. A multi-level computational model for multi-scale damage analysis in composite and porous materials. Int J Sol Struct. 2001;38(14):2335–2385.
[33] Ghosh S, Lee K, Moorthy S. Multiple scale analysis of heterogeneous elastic structures using homogenization theory and voronoi cell finite element method. Int J Sol Struct. 1995;32 (1):27–62.
[34] Borkowski LB, Liu KC, Chattopadhyay A. From ordered to disordered: the effect of microstructure on composite mechanical performance. CMC Comput Mater Contin. 2013;37:161–193.
[35] Johnston JP, Koo B, Subramanian N, et al. Modeling the molecular structure of the carbon fiber/polymer interphase for multiscale analysis of composites. Compos B Eng. 2017;111:27–36.
[36] Gao YC, Mai YW, Cotterell B. Fracture of fiber-reinforced materials. Z Angew Math Phys. 1988;39(4):550–572.
[37] Hutchinson JW, Henrik MJ. Models of fiber debonding and pullout in brittle composites with friction. Mech Mater. 1990;9(2):139–163.
[38] Zhou LM, Kyo KJ, Wing MY. Interfacial debonding and fibre pull-out stresses. J Mater Sci. 1992;27(12):3155–3166.
[39] Chai YS, Wing MY. New analysis on the fiber push-out problem with interface roughness and thermal residual stresses. J Mater Sci. 2001;36(8):2095–2104.
[40] Zhou LM, Wing MY. A new model for evaluation of the interfacial friction coefficient and residual clamping stress in a fiber-push-out test. Philos Mag Lett. 1993;68(1):5–11.
[41] Zhou L, Kim JK, Baillie C, et al. Fracture mechanics analysis of the fiber fragmentation test. J Compos Mater. 1995;29(7):881–902.
[42] Jero PD, Kerans RJ. The contribution of interfacial roughness to sliding friction of ceramic fibers in a glass matrix. Scrip Mater. 1990;24(12):2315–2318.
[43] Carter WC, Fuller JER, Butler EP. Micro-mechanical aspects of asperity-controlled friction in fiber-toughened ceramic composites. Scrip Mater. 1991;25(3). DOI:10.1016/0956-716X (91)90095-I
[44] Kerans RJ, Parthasarathy TA. Theoretical analysis of the fiber pullout and pushout tests. J Am Ceram Soc. 1991;74(7):1585–1596.
[45] Parthasarathy TA, Marshall DB, Kerans RJ. Analysis of the effect of interfacial roughness on fiber debonding and sliding in brittle matrix composites. Acta Mater. 1994;42 (11):3773–3784.
[46] Parthasarathy TA, Barlage DR, Jero PD, et al. Effect of interfacial roughness parameters on the fiber pushout behavior of a model composite. J Am Ceram Soc. 1994;77(12):3232–3236.
[47] Mackin TJ, Jingyu Y, Warren PD. Influence of fiber roughness on the sliding behavior of sapphire fibers in Ti-Al and glass matrices. J Am Ceram Soc. 1992;75(12):3358–3362.
[48] Mackin TJ, Warren PD, Evans AG. Effects of fiber roughness on interface sliding in composites. Acta Mater. 1992;40(6):1251–1257.
[49] Verma A, Parashar A, Packirisamy M. Effect of grain boundaries on the interfacial behaviour of graphene-polyethylene nanocomposite. Appl Surf Sci. 2019;470:1085–1092.
[50] Verma A, Parashar A, Packirisamy M. Atomistic modeling of graphene/hexagonal boron nitride polymer nanocomposites: a review. Wiley Interdiscip Rev Comput Mol Sci. 2018;8 (3):e1346.
[51] Lu CT, Weerasinghe A, Maroudas D, et al. A comparison of the elastic properties of graphene-and fullerene-reinforced polymer composites: the role of filler morphology and size. Sci Rep. 2016;6(1):1–9.

[52] Rahman R, Foster JT. Deformation mechanism of graphene in amorphous polyethylene: a molecular dynamics-based study. Comput Mater Sci. 2014;87:232–240.
[53] Mattsson TR, Lane JM, Cochrane KR, et al. First-principles and classical molecular dynamics simulation of shocked polymers. Phys Rev B. 2010;81(5):054103.
[54] Odegard GM, Jensen BD, Gowtham S, et al. Predicting mechanical response of crosslinked epoxy using ReaxFF. Chem Phys Lett. 2014;591:175–178.
[55] Liu L, Liu Y, Zybin SV, et al. ReaxFF-lg: correction of the ReaxFF reactive force field for London dispersion, with applications to the equations of state for energetic materials. J Phys Chem A. 2011;115(40):11016–11022.
[56] Liu HY, Min ZL, Wing MY. On fiber pull-out with a rough interface. Philos Mag (Abingdon). 1994;70(2):359–372.
[57] Liu HY, Min ZL, Wing MY. Effect of interface roughness on fiber push-out stress. J Am Ceram Soc. 1995;78(3):560–566.
[58] Stupkiewicz S. Fiber sliding model accounting for interfacial micro-dilatancy. Mech Mater. 1996;22(1):65–84.
[59] Parthasarathy TA, Kerans RJ. Predicted effects of interfacial roughness on the behavior of selected ceramic composites. J Am Ceram Soc. 1997;80(8):2043–2055.
[60] Verma A, Kumar R, Parashar A. Enhanced thermal transport across a bi-crystalline graphene–polymer interface: an atomistic approach. Phys Chem Chem Phys. 2019;21(11):6229–6237.
[61] Jager J, Will JM, Horn S. Determination of nano-roughness of carbon fibers by atomic force microscopy. J Mater Sci. 2013;48(19):6803–6810.
[62] Sharma M, Gao S, Mader E, et al. Carbon fiber surfaces and composite interphases. Compos Sci Technol. 2014;102:35–50.
[63] Vautard F, Fioux P, Vidal L, et al. Influence of the carbon fiber surface properties in interfacial adhesion in carbon fiber-acrylate composites cured by electron beam. Compos Part A Appl Sci Manuf. 2011;42:859–867.
[64] Li C, Xian G. Influence of elevated temperature treatment on the microstructures and mechanical properties of carbon fibers in argon environment. J Mater Eng Perform. 2019;28(12):7804–7815.
[65] Nohara LB, Filho GP, Nohara EL, et al. Evaluation of carbon fiber surface treated by chemical and cold plasma processes. Mater Res. 2005;8(3):281–286.
[66] Liu W, Gao Y, Liu X, et al. Tensile and interfacial properties of dry-jet wet-spun and wet-spun polyacrylonitrile-based carbon fibers at cryogenic condition. J Eng Fiber Fabr. 2019;14:1–8.
[67] Zhao F, Huang Y. Grafting of polyhedral oligomeric silsesquioxanes on a carbon fiber surface: novel coupling agents for fiber/polymer matrix composites. J Mater Chem. 2011;21(11):3695–3703.
[68] Xiong QL, Tian XG. Atomistic modeling of mechanical characteristics of cnt-polyethylene with interfacial covalent interaction. J Nanomater. 2015;2015:237520.
[69] Ma J, Rokhlin V, Wandzura S. Generalized Gaussian quadrature rules for systems of arbitrary functions. SIAM J Numer Anal. 1996;33(3):971–996.
[70] van Duin ACT, Dasgupta S, Lorant F, et al. ReaxFF: a reactive force field for hydrocarbons. J Phys Chem A. 2001;105(41):9396–9409.
[71] Fan D, Lue L, Yang S. Molecular dynamics study of interfacial stress transfer in graphene-oxide cementitious composites. Comput Mater Sci. 2017;139:56–64.
[72] Liu F, Hu N, Ning H, et al. Molecular dynamics simulation on interfacial mechanical properties of polymer nanocomposites with wrinkled graphene. Comput Mater Sci. 2015;108:160–167.
[73] Jin Y, Duan F, Mu X. Functionalization enhancement on interfacial shear strength between graphene and polyethylene. Appl Surf Sci. 2016;387:1100–1109.
[74] Yang Y, Zhao Y, Li Y, et al. Effect of sizing on the interfacial shear strength of carbon fiber/epoxy resin monofilament composite. J Wuhan Univ Technol Mater Sci Ed. 2014;29(3):483–487.